J Am Ceram Soc. 2026;109:e70247
https://doi.org/10.1111/jace.70247

Silica-assisted cold sintering of diopside for sustainable cementitious composites

Wei Huang [a,b], Jingjing Yang [a,b], Boya Li [b], Mingjiang Tao [c], Guoping Zhang [d], Jian Luo [a,b,*]

[a] *Aiiso Yufeng Li Family Department of Chemical and Nano Engineering, University of California San Diego, La Jolla, CA 92093, USA.*

[b] *Program in Materials Science and Engineering, University of California San Diego, La Jolla, CA 92093, USA.*

[c] *Department of Civil, Environmental, & Architectural Engineering, Worcester Polytechnic Institute, MA 01609, USA.*

[d] *Department of Civil and Environmental Engineering, University of Massachusetts Amherst, Amherst, MA 01003, USA.*

Abstract

This study explores cold sintering of naturally occurring minerals as supplementary cementitious materials (SCM) or cement analogs, which have the potential to transform the traditional high-energy, high-emission cement manufacturing pathways. Diopside ($MgCaSi_2O_6$), a natural inosilicate, is used as the model system. As diopside is hard for cold sintering directly (by itself), this study demonstrates that the addition of amorphous silica nanoparticles can enable cold sintering of diopside. The cold sintered diopside-silica composites are characterized by X-ray diffraction, scanning electron microscopy, and transmission electron microscopy. The effect of the relative weight percentage of silica added is examined. The relative density of the cold sintered composite reaches nearly 90% at 400 MPa and 200 °C in 60 min. For specimens with the addition of 30 wt% or more of amorphous SiO_2, cold sintering also induces partial crystallization, converting a fraction of amorphous silica to quartz. The crystallization kinetics exhibits a stochastic nature. The Vickers hardness of the cold-sintered diopside-silica composite increases with increasing the amount of silica that promotes cold sintering, reaching ~3 GPa with 20 wt% or more silica. The diopside-silica composites studied here serve as a model system for leached silicate mine tailings, which are expected to have nanoporous amorphous silica shells on silicate particles to enable the silica-assisted cold sintering mechanism discovered in this study.

Keywords: Cold sintering; Diopside; Silicate; Silica; Densification

[*] Corresponding author: J. Luo, 9500 Gilman Drive, Mail Code 0448, University of California San Diego, La Jolla, CA 92093, USA. *Email address:* jluo@alum.mit.edu

1. Introduction

Ordinary Portland cement (OPC) is by far the world's most widely used manufactured material.[1] However, its production is not environmentally friendly due to the high energy demand (*e.g.*, ~5000 MJ is consumed to produce 1.0 ton OPC), consumption of non-renewable resources (*e.g.*, production of 1.0 ton OPC consumes ~1.5 ton limestone and clay), and substantial CO_2 emissions (*e.g.*, ~0.95 ton CO_2 per 1.0 ton OPC).[2] Consequently, cement production accounts for 7% of global anthropogenic CO_2 emissions, marking it as a critical target for decarbonization and calling for novel materials science to find substitute materials and manufacturing processes.[3] Therefore, eco-friendly manufacturing technologies of next-generation, low-carbon cement and supplementary cementitious materials (SCM) are urgently needed. Mine tailings, the pulverized mining wastes, have gained increasing attention as alternative raw materials for producing environmentally sustainable cementitious materials due to their high amounts of silicates and aluminates. In addition, carbonation of mine tailings is emerging as a promising approach for decarbonization. This process begins with the dissolution of magnesium (Mg^{2+}) and calcium (Ca^{2+}) from the silicate,[4–6] forming a passivated layer typically composed of amorphous silica on the silicate surface.[7] Mineral carbonation offers a dual benefit: not only does it sequester CO_2, but it also has the potential to produce alternative cementitious materials.[8] As the first step to explore these possibilities and demonstrate the feasibility, herein we investigate a model system using diopside ($MgCaSi_2O_6$) and amorphous silica to mimic the leached silicate mine tailings (silicates with surface nanoporous amorphous silica layers) to generate cementitious materials by novel cold sintering techniques (discussed below). Diopside is selected as a representative silicate due to its compositional similarity to natural mine tailing minerals. While it serves as the model phase here, the silica-assisted cold sintering strategy is expected to be applicable to a broader range of silicate-based materials. Specifically, it can be applied to leached mine tailings and further combined mineral carbonization in future studies.

Recently, a cold sintering process has garnered increasing attention for its ability to densify various ceramics,[9–12] solid-state electrolyte,[13–15] ferroelectrics,[16–18] and semiconductors[19,20] at low temperatures. While conventional ceramic sintering typically requires temperatures corresponding to 50–95% of a material's melting point, cold sintering achieves densification at only 10–20% of that temperature range,[21] thereby offering substantial energy and cost savings. This low-temperature densification is driven by a dissolution–reprecipitation mechanism, wherein a transient liquid phase and uniaxial pressure facilitate particle rearrangement and densification.[10,16] Recent studies have extended cold sintering to silica-based materials, including silica,[22,23] silica-PTFE composite,[24] diatomaceous earth,[25] soda-lime glass,[26] and transparent silica glass,[27] often requiring alkaline conditions to promote silica dissolution. In an analogy, cold sintering was a promising alternative manufacturing technology for cementitious materials because it resembles natural geological processes in which a ceramic powder is densified under a combination of liquid-phase mediation, intense external pressure, and mild temperature.[28]

In this study, we investigate the cold sintering of diopside-silica composites as a model system (mimic leached silicate mine tailings with surface amorphous silica layers on silicate particles). By introducing 30–50 nm amorphous silica nanoparticles, we achieved a relative density increase from 70% (pure diopside) to nearly 90%, demonstrating the feasibility to densify silicate-based materials at a low temperature of 200 ℃. Mechanical testing revealed a corresponding enhancement in Vickers hardness scaling with SiO_2 content that promotes cold sintering. At higher silica addition (≥30 wt%), partial crystallization of amorphous silica to form dispersed quartz crystals enhanced mechanical reinforcement, but it introduced microstructural inhomogeneity. The interplay between SiO_2 crystallization dynamics and densification pathways may offer a pathway to tailor microstructures. This study demonstrated a silica-assisted cold sintering mechanism for diopside, wherein silica content, crystallization kinetics, and densification mechanisms collectively govern material processing and the final microstructures, which in turn affect properties (*e.g.*, hardness and other mechanical properties).

In a broader context, densification and cementation, the major strengthening processes in cold sintering, can entail a series of fundamental mechanisms: particle rearrangement and packing, interfacial diffusion and grain boundary healing, mechanical interlocking, dissolution-precipitation, and hydrothermal reactions. The acting mechanisms can be material-specific and depend on sintering parameters. An additional objective of this study is to investigate the microstructural evolution and crystallization during cold sintering of diopside-silica composites to probe the processing-microstructure-property relationship.

2. Materials and Methods

2.1 Powder preparation

Commercially available diopside powder (Vibrancys, India) with an initial particle size of 500-900 μm and amorphous silica (a-SiO_2) powder (30-50 nm, US Research Nanomaterials, Texas, USA) were used as the starting materials. To reduce the particle size, the as-received diopside powder was planetary ball-milled at 300 rpm for 24 h with isopropyl alcohol. The resulting slurry was oven-dried at 60 ℃ for 24 h. The dry milled diopside powder (Figure S1A in the Supplementary Material) was then mixed with a-SiO_2 powder (Figure S1B and C in the Supplementary Material) at different weight percentages: $MgCaSi_2O_6 + x \cdot SiO_2$, where x = 0 wt% (nominally pure $MgCaSi_2O_6$), 10 wt%, 20 wt%, 30 wt%, 40 wt%, and 50 wt%, respectively. The mixture powders were vortexed for 5 min for homogenization before cold sintering.

2.2 Cold sintering

For each sample, 0.23 g of the $MgCaSi_2O_6 + x \cdot SiO_2$ powder was mixed with 30 wt% of a NaOH solution (prepared using a 10.0 M NaOH stock, Sigma-Aldrich, USA). 2M NaOH solutions were used for cold sintering by default, while 1 M and 5 M NaOH solutions were also tested. The mixture was hand-ground using an agate mortar and pestle and then loaded into a 10 mm pressing

die. The die was pressed at 400 MPa using a Carver press. A band heater was used to heat the die to 200 °C at a heating ramp rate of 10 °C/min. The sample was held at the constant pressure (400 MPa) and temperature (200 °C) for up to 60 min. Subsequently, the cold sintered pellets were dried in an oven at 60 °C overnight to remove any residual moisture.

2.3 Characterization

X-ray diffraction (XRD) patterns were acquired with a Rigaku Miniflex II diffractometer operating at 30 kV and 15 mA, in a continuous scan mode with Cu Kα radiation. The XRD patterns were obtained with a step size of 0.02° and a scan speed of 2°/min. The XRD spectra were analyzed by GSAS II. Rietveld refinements were performed. XRD refinement results for nine specimens are documented in Figure S2 in the Supplementary Material.

The initial powders and sintered specimens were characterized by scanning electron microscopy (SEM) using an FEI Apreo microscope and transmission electron microscopy (TEM) using a Thermofisher Talos 200X microscope.

The density of sintered pellets was measured using the Archimedes method. The theoretical densities of the cold sintered pellets were calculated based on the total SiO_2 amount added and the crystalline phase fractions computed by XRD Rietveld refinements.

2.4 Hardness measurements

Vickers hardness (GPa) was measured using a LECO micro hardness testing machine under a load of 0.5 kgf (for a holding duration of 10 s), abiding by ASTM Standard C1327. Sixty indentations were performed per sample at different locations for each specimen to ensure statistical validity and average local microstructural effects. Cracks and pores were excluded from indentation measurements. Examples of indents are shown in Figure S6 in the Supplementary Material.

3. Results and discussion

3.1 Silica-assisted cold sintering of diopside

Following 24 h of ball milling, the diopside ($MgCaSi_2O_6$) powder exhibited a broad particle size distribution (from ~500 nm to ~3 μm) with irregular morphologies, including fine particles, rod-shaped aggregates, and angular fragments, as shown in Figure S1A in the Supplementary Material. As cold sintering of pure diopside powders could only achieve ~70% relative density (with little densification), 10-50 wt% of 30–50 nm amorphous silica (a-SiO_2) nanoparticles were added to facilitate cold sintering of diopside; see SEM and TEM images of these a-SiO_2 nanoparticles in Figure S1B and Figure S1C, respectively, in the Supplementary Material.

The cold sintering results of pure diopside using different solvents, including DI water, 2M acetic acid and 2M NaOH all exhibited limited densification (<73% relative density, Supplementary Table S1), indicating insufficient dissolution of diopside under both acidic and

alkaline conditions. This may be attributed to the formation of a surface passivation layer during the initial dissolution stage, which inhibits further dissolution and limits densification.[7] With the addition of 30-50 wt% SiO_2 in $MgCaSi_2O_6$, ~90% relative densities were achieved after cold sintering (using 2 M NaOH and 60-min hold at 200 °C and 400 MPa, which represents our standard cold sintering conditions).

Presumably, the introduction of these silica nanoparticles facilitated particle rearrangement and promoted dissolution-precipitation kinetics during cold sintering (with the expected high dissolution rates of silica in an alkaline solution). Here, we note that the diopside-silica mixtures resemble (serves as a model system for) leached silicate mine tailings, where shells of nanoporous amorphous silica are expected form on silicate particles. This study demonstrated the feasibility of a-SiO_2 enabled cold sintering of $MgCaSi_2O_6$ and potentially other silicates.

3.2 Crystallization of amorphous silica (a-SiO_2)

XRD analysis of $MgCaSi_2O_6$-SiO_2 composites (Figure 1A) revealed that all peaks in samples with 10-20 wt% SiO_2 can be indexed to the diopside phase without detectable secondary crystalline phase, which indicated that the SiO_2 remained amorphous after cold sintering. In specimens with 30-50 wt% SiO_2, distinct alpha (α) quartz (crystallized SiO_2 with space group $P3_221$) peaks emerged, indicating crystallization of amorphous silica during cold sintering. This observation is in align with prior studies reporting amorphous-to-quartz transformations during cold sintering of pure a-SiO_2.[23,24]

Notably, specimens with the identical nominal amount of SiO_2 displayed different fractions of the crystalline quartz phase for batches containing 30-50 wt% of SiO_2, indicating the stochastic nature of the crystallization process (presumably stochastic quartz nucleation). To show this variability, samples from the same given amount of SiO_2 were labeled as either a high crystallization fraction (HCF) or a low crystallization fraction (LCF) based on the measured quartz content.

To further investigate crystallization kinetics, $MgCaSi_2O_6$ + 30 wt% SiO_2 samples were cold sintered with varying dwell times at 200 °C and 400 MPa. XRD analysis (Figure 1C) revealed that the crystallized quartz phase became detectable only at and after 50 minutes, suggesting that crystallization predominantly occurred during the later stage of cold sintering. Although the relative density appears to plateau around 40 min (Figure 2C), subsequent analysis (Figure S4) indicates that densification continues beyond this point, likely compensating for the porosity generated by the volume shrinkage caused by quartz crystallization. These results also indicate that quartz nucleation requires a long incubation time. In addition to the incubation behavior, variations in quartz crystallinity were observed among specimens with the same nominal SiO_2 content and sintering conditions. Such variations could arise from local inhomogeneities in amorphous silica distribution, which may influence dissolution and crystallization kinetics. Previous studies have shown that crystallization of amorphous silica during cold sintering is sensitive to processing conditions. Prior studies also suggested that partial transformation to quartz

occurred only under sufficiently alkaline environments and with specific temperature profiles.[23,24,29] In contrast, some silica systems remained fully amorphous after cold sintering in comparable conditions.[22] These findings suggest that local microstructural or chemical variations, even under identical globally conditions, may lead to significant differences in crystallization behaviors.

3.3 Cold sintering kinetics: the effects of silica content and dwell time

As shown in Figure 2A, the measured bulk densities, which showed a large sample-to-sample variation for a given SiO_2 content, initially increased with SiO_2 addition but declined beyond 30 wt%, attributable to the lower density of quartz (2.65 g/cm³) relative to diopside (3.28 g/cm³). The fractions of crystallized quartz were quantified via Rietveld refinements (Figure 2A, Table 1), which correlated with the SiO_2 content but with a large sample-to-sample variation due to the stochastic nature of crystallization. Fluctuations in measured densities at high SiO_2 content (≥30 wt%) arose from sample-to-sample variation in SiO_2 crystallization fractions. In Figure 2A, the color bar represents the fraction of amorphous silica that crystallized into quartz during the cold sintering process, relative to the total amount of amorphous silica initially added. This additional variable helps visualize the sample-to-sample variation in crystallization, which contributes to the density fluctuations observed at higher SiO_2 contents. The large variation in measured densities is because quartz has a higher density than amorphous silica; thus, for samples with comparable porosity, a higher fraction of crystallized quartz leads to an increased bulk density. When the crystallization extent varies stochastically among samples with the same nominal composition, it introduces measurable variations in the absolute densities. This explains the large variation in the measured absolute densities, which reduces significantly in relative densities (as discussed below), for high-silica specimens despite identical sintering conditions.

In addition, a variation in measured densities was also observed for the specimens with 10 wt% SiO_2, which likely resulted from inhomogeneous dispersion of a-SiO_2 nanoparticles during mixing (at this low SiO_2 content).

Relative densities (Figure 2B), calculated based on the theoretical density obtained using the Rietveld refined crystalline phase fractions and the nominal SiO_2 contents, shewed more consistent values for a given SiO_2 content (particularly for specimens containing 30-50 wt% SiO_2, after accounting for volume change due to the SiO_2 crystallization of different fractions), implying crystallization does not affect relative sintered densities significantly. Notably, smaller sample-to-sample variations were observed in the calculated relative densities for specimens containing 30-50 wt% SiO_2 (represented by small error bars in Figure 2B); thus, the large sample-to-sample variations in measured true densities were mostly due to the stochastic crystallization in these specimens with high SiO_2 contents.

To further assess whether the crystallization of amorphous silica affects the cold sintering densification, the relative densities of specimens containing 30–50 wt% SiO_2 were plotted against the fraction of quartz crystallized, normalized to the total amount of amorphous silica added

(Figure S3). The absence of a clear negative correlation indicates that the transformation from amorphous silica to quartz does not reduce relative density.

The effect of hold time on densification during cold sintering was further examined with $MgCaSi_2O_6$ + 30 wt% SiO_2 specimens. Although the relative density appeared to plateau after ~40 min dwell (Figure 2C), quartz crystallization from amorphous silica began during this stage, and cold sintering densification likely continued afterward (according to the analysis in Supplementary Figure S4 and further discussed below).

Notably, the crystallization induced volume shrinkage of the SiO_2 to generate porosity, but the overall porosity remains largely unchanged (with a small increase at 60 min, as shown in Figure S4). The porosity generated as a result of crystallization induced volume shrinkage was estimated based on the molar volume difference between amorphous silica and quartz. The overall porosity was determined as the complement of relative density. Supplementary Figure S4 implies that the porosity generated by crystallization is subsequently removed by continued densification. If no further densification occurred, samples with more quartz would exhibit greater porosity or lower relative density (or the porosity should increase and relative density should decrease with crystallization), which was not observed. Therefore, cold-sintering densification and crystallization are not strictly sequential processes. Instead, they are partially coupled. The cold sintering process still take place to reduce porosity after the onset of quartz crystallization, and the two kinetic processes can interplay. This insight offers a new understanding of the time-dependent cold sintering in silicate systems with crystallization.

3.4 The effects of pH

It is known that sodium hydroxide solutions (in comparison with water) can promote the silica dissolution and depolymerization rate.[30] To assess pH effects on silica dissolution, NaOH concentrations (1–5 M) were tested (Figure 2D). Minimal densification occurred when a 1 M NaOH solution was used, but the relative densities leveled off at 2–5 M NaOH. This observation indicates that pH affects cold sintering kinetics, with a threshold beyond which increased alkalinity no longer accelerates sintering. This suggests that while higher NaOH concentrations enhance cold sintering (presumably via enhancing silica dissolution), densification is constrained by other kinetic or thermodynamic factors after the pH reaches a threshold (in ≥ 2M NaOH solutions).

In contrast to the current system, previous studies on zeolite-based systems reported enhanced densification with increasing NaOH concentration, attributed to more reactive Al–O–Si bonds that allows for continuous dissolution and recrystallization as NaOH concentration increases.[31] In the present diopside–silica composite system, densification is primarily enabled by the dissolution of amorphous silica at moderate NaOH concentration. At high NaOH concentrations (≥5 M), excessive alkalinity may promote surface passivation around diopside particles, thereby hindering effective densification. This comparison highlights the material specific role of solution chemistry in cold sintering, depending on the dissolution behavior of the reactive phase involved.

Based on the observations shown above, a schematic summary of the sequence of kinetic processes is illustrated in Figure 3. Initially, diopside and amorphous silica particles are wetted by the NaOH solution, where the liquid phase promotes particle rearrangement and facilitates the redistribution of finer silica particles to fill the interstitial spaces between the larger diopside. Once the pressure and temperature are applied, the dissolution and reprecipitation process of amorphous silica can happen, while solvent is evaporating, leaving an intergranular glassy phase. With continue holding at 200 °C for an incubation period exceeding ~40 min, the cold-sintering densification completes and interplay with (partial) crystallization of amorphous silica into quartz in a stochastic manner, resulting in a heterogeneous composite consisting of diopside, residual amorphous silica, and newly formed α-quartz.

3.5 Microstructures

The microstructures of the cold sintered $MgCaSi_2O_6$-SiO_2 composites, as revealed by SEM characterization of fractured surfaces (Figure 4) and polished cross-sections (Figure 4), demonstrate a clear dependence on silica content.

On the fractured surfaces, pure diopside exhibited no interparticle necking, with a microstructure dominated by loosely compacted particles (Figure 4A), indicative of no substantial sintering. With 10 wt% silica addition (Figure 4B), minimal densification occurred, though the (inhomogeneous) "coating" of (30–50 nm) a-SiO_2 nanoparticles on diopside surfaces, forming a discontinuous network. At intermediate silica contents (20 wt%), a continuous a-SiO_2 matrix phase developed, with nanosized pores (Figure 4C). Further increasing silica to 30–50 wt% (Figure 4D-F) triggered the nucleation of polygonal (faceted) quartz grains within the matrix, consistent with the amorphous-to-quartz crystallization observed in XRD (Figure 1A).

Cross-sectional backscattered electron (BSE) SEM images (Figure 5) further elucidated trends of composition-dependent porosity. Low-magnification images of the $MgCaSi_2O_6$ + 30 wt% SiO_2 composite revealed abundant elongated macropores (>5 μm) aligned perpendicular to the applied uniaxial pressure direction, a result of anisotropic particle rearrangement during pressing. These large pores stemmed from particle packing heterogeneity, exacerbated by inadequate mixing and the irregular morphology of diopside particles. In contrast, samples with higher silica content (40–50 wt%) exhibited reduced macroporosity but localized pore clusters retained (Figure 5E–L). High-magnification images (Figure 5A, E and I) identified submicron (<1 μm) pores surrounded by needle-shaped quartz grains, confirming pore formation via volumetric shrinkage during silica crystallization. The non-uniform densification observed across all compositions further underscores the influence of insufficient precursor mixing on the final microstructure.

TEM images (Figure 6A-D), along with fast Fourier transform (FFT) image analysis (Figure 6A–D), further resolved nanoscale phase distribution. Diopside particles were embedded within a matrix of quartz and amorphous silica, with FFT patterns confirming the coexistence of crystalline quartz and diopside and amorphous silica (Figure 6B–D). To further examine the local chemical environment, EDS elemental mapping was performed on a representative region using a scanning

TEM (STEM) mode. As shown in Figure S5, Ca and Mg signals are confined to individual grains, while Si is more broadly distributed. This indicates that the amorphous silica phase remains intergranular after cold sintering. This observation supports the densification mechanism dominated by silica dissolution and reprecipitation.

3.6 Hardness

Vickers hardness testing was performed on defect-free regions of the composites under a 0.5 kgf (4.9 N) load to ensure measurement accuracy. Figure S6 in the Supplementary Material shows secondary electron SEM images of indentation morphologies in a dense, crack-free zone (Figure S6A) and a region adjacent to a horizontal crack (Figure S6B). In the latter case, pre-existing cracks induced radial crack propagation and material spallation, distorting indentation geometry and invalidating measurements (Figure S6B), whereas defect-free regions yielded well-defined indentations for reliable hardness measurements (Figure S6A).

The trend in measured hardness (Figure 7) correlates strongly with SiO_2 content and the relative densities after cold sintering (Figure 2B). Samples containing ≤10 wt% SiO_2 exhibited low hardness (<2 GPa), attributed to high porosity and poor densification. Increasing SiO_2 content (20–50 wt%) enhanced hardness (2.9 – 3.5 GPa) due to less porosity (better sintered specimens) and quartz crystallization, which reinforced the amorphous SiO_2 matrix phase. However, significant fluctuations existed at higher SiO_2 concentrations (with a large variation in measured hardness values for the specimen containing 50 wt% SiO_2, as indicated by a larger error bar in Figure 6 representing the standard deviation from 60 indents), reflecting the effects of microstructural inhomogeneity from stochastic SiO_2 crystallization and residual submicron pores (see, *e.g.*, Figure 5A, E, and I). These observations highlight the dual role of SiO_2 crystallization: improving hardness via crystallization, while increasing microstructural inhomogeneity and sample-to-sample variation.

4. Conclusions

This study demonstrated cold sintering of diopside-based composites enabled by the addition of amorphous silica nanoparticles. The addition of amorphous silica enhanced particle packing and served as a “glue” phase via promoting dissolution-precipitation kinetics in silica to enable and promote cold sintering. High silica content (30–50 wt%) induced partial crystallization of a-SiO_2 at ≥ ~50 min, where the relative density largely leveled off (as the porosity generated by the molar volume shrinkage due to crystallization of silica compensated the cold-sintering densification). Rietveld refinements revealed that stochastic nature of crystallization with sample-to-sample variations in quartz fractions, which caused scattered measured densities but with much smaller sample-to-sample variations in the relative densities. TEM analysis confirmed the coexistence of diopside, quartz, and amorphous phases, with submicron pores. Measured Vickers hardness values correlated well with the SiO_2 content and relative density. While NaOH concentrations ≥2 M facilitated silica dissolution to promote cold sintering, a higher concentration did not enhance

density further. These findings underscore the potential to tailor microstructures and properties by controlling cold sintering and crystallization kinetics.

The diopside-silica composites studied here serve as a model system for leached silicate mine tailings, which are expected to have amorphous silica shells on silicate particles to enable silica-assisted cold sintering mechanism discovered in this study. While diopside is used here as a prototypical silicate, the cold sintering mechanism can in principle be applied to other inorganic silicates or mine tailing analogs. To assess the generality and robustness of this silica-assisted approach, future work will explore cold sintering of a variety of alternative materials. Ongoing studies will focus on leached mine tailings and the integration of cold sintering with various leached mine tailings, along with carbonation of leached Ca^{2+} and Mg^{2+} ions, to explore manufacturing pathways to transform the traditional high-energy, high-emission cement. This study of cold sintering of diopside-silica model system offers the first step and a feasibility test towards this long-range goal.

Acknowledgment

The study was supported by the U.S. National Science Foundation (NSF) Future Manufacturing Research Grant (FMRG) program (Award No. CBET-2328044).

Table 1. Measured crystallized quartz fractions (normalized to the total SiO_2 added) and true, theoretical, and relative densities of cold sintered samples with 30-50 wt% silica additions, which were obtained based on Rietveld refinements of XRD patterns.

Sample	Quartz Fraction (%)	Density (g/cm^3)	Theoretical Density (g/cm^3)	Relative Density (%)
$MgCaSi_2O_6$ + 30 wt% SiO_2 #1 (LCF)	6	2.54	2.87	88.6
$MgCaSi_2O_6$ + 30 wt% SiO_2 #2 (HCF)	69	2.60	2.99	87.0
$MgCaSi_2O_6$ + 30 wt% SiO_2 #3 (HCF)	66	2.63	2.99	88.1
$MgCaSi_2O_6$ + 40 wt% SiO_2 #1 (LCF)	4	2.46	2.75	89.4
$MgCaSi_2O_6$ + 40 wt% SiO_2 #2 (HCF)	50	2.56	2.86	89.5
$MgCaSi_2O_6$ + 40 wt% SiO_2 #3 (HCF)	64	2.64	2.90	91.2
$MgCaSi_2O_6$ + 50 wt% SiO_2 #1 (LCF)	38	2.42	2.74	88.2
$MgCaSi_2O_6$ + 50 wt% SiO_2 #2 (HCF)	93	2.57	2.91	88.5
$MgCaSi_2O_6$ + 50 wt% SiO_2 #3 (HCF)	85	2.61	2.88	90.6

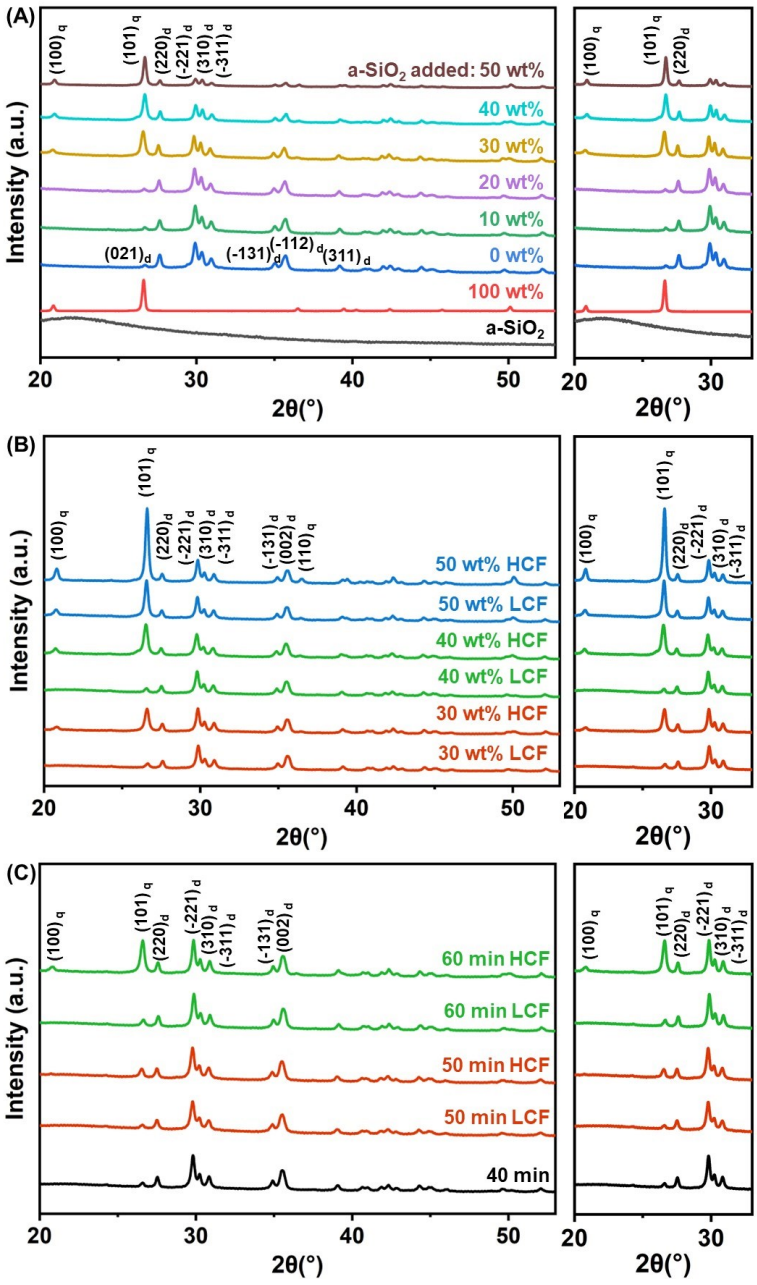

Figure 1. (A) X-ray diffraction (XRD) of cold sintered diopside with the addition of different weight percents of silica (SiO_2) with 60-min hold at 200 °C and 400 MPa. XRD patterns of cold sintered specimens with varying amounts of crystallized quartz with (B) different weight percentages of SiO_2 added with 60-min hold, and (C) with varying hold times in the $MgCaSi_2O_6$ + 30 wt% SiO_2 specimens. The phases are identified as: *q* = quartz, *d* = diopside. Note that crystallization has stochastic nature for specimens with 30 wt% or more a-SiO_2 additions, where HCF and LCF represent specimens with the high and low crystallization fractions, respectively, at the nominally identical cold sintering conditions.

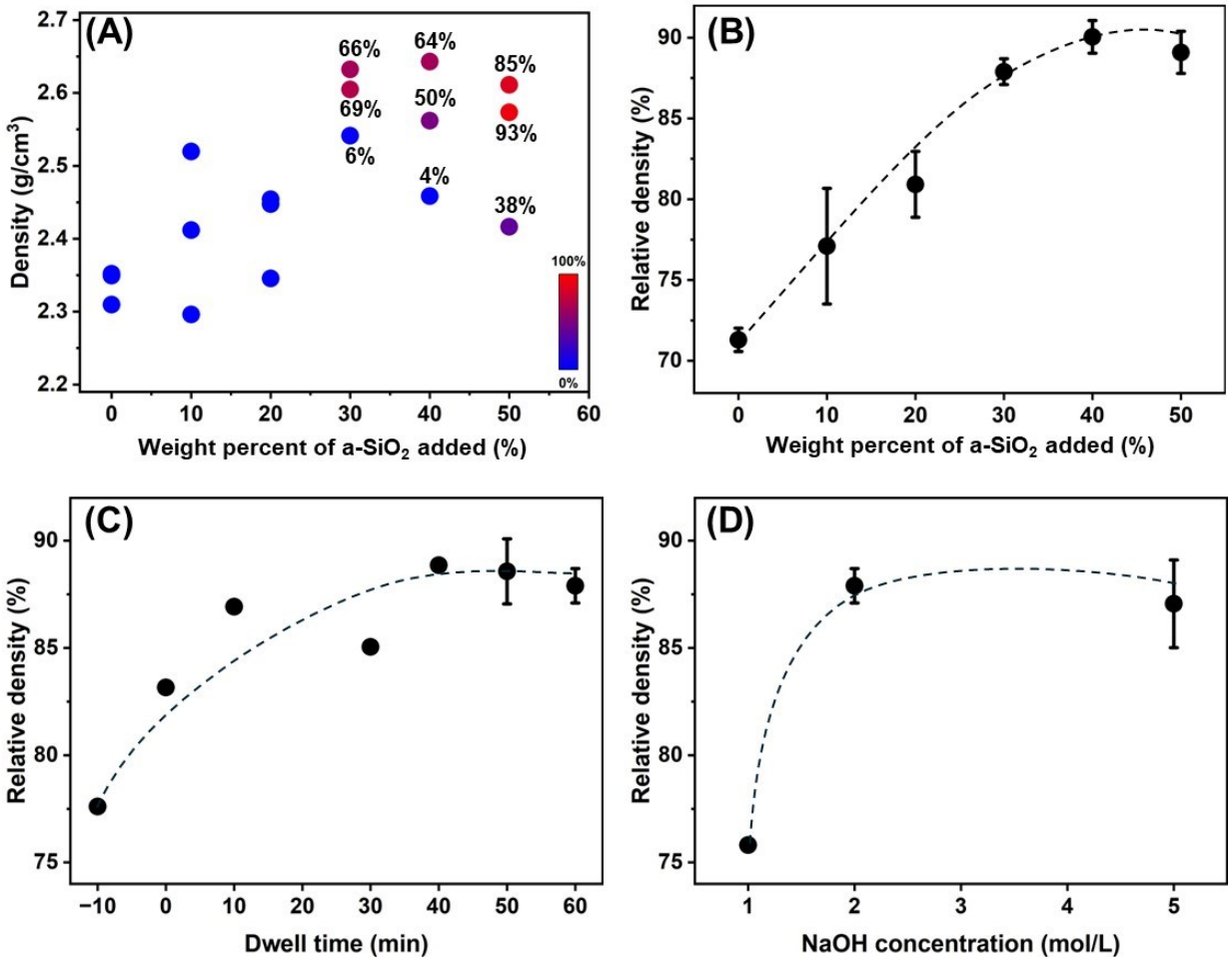

Figure 2. Measured (A) densities and (B) relative densities of $MgCaSi_2O_6$ with different weight percentages of silica added (2 M NaOH and 60-min hold). Relative density of $MgCaSi_2O_6$ + 0.3 wt% SiO_2 *vs.* (C) dwell time after reaching 200 °C (using 2 M NaOH; the heating ramp rate was 10 °C/min prior to reaching 200 °C) and (D) NaOH concentration (for 60-min hold) curves. The color bar in panel (A) indicates the fraction of amorphous silica that crystallized into quartz during the cold sintering process, normalized to the total amount of amorphous silica initially added.

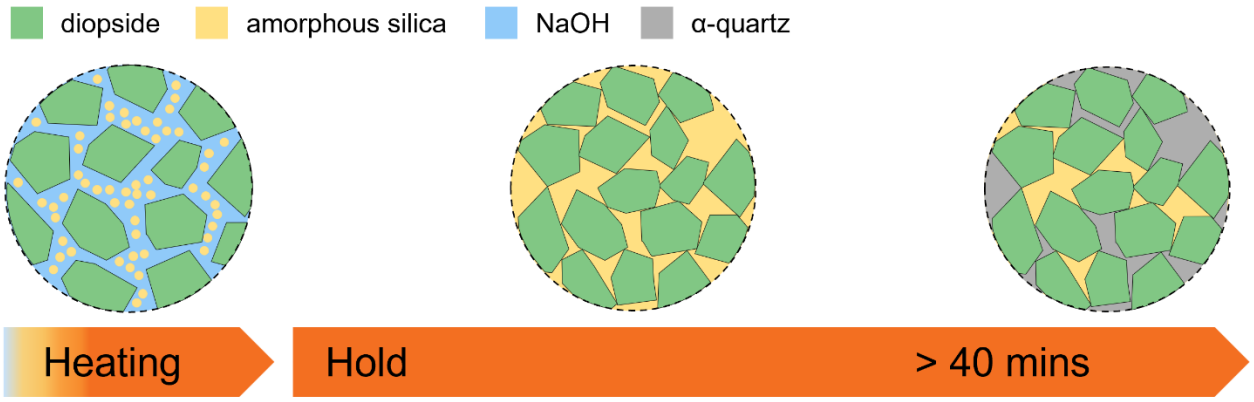

Figure 3. Schematic illustration of the stages during the cold sintering of diopside-silica composite.

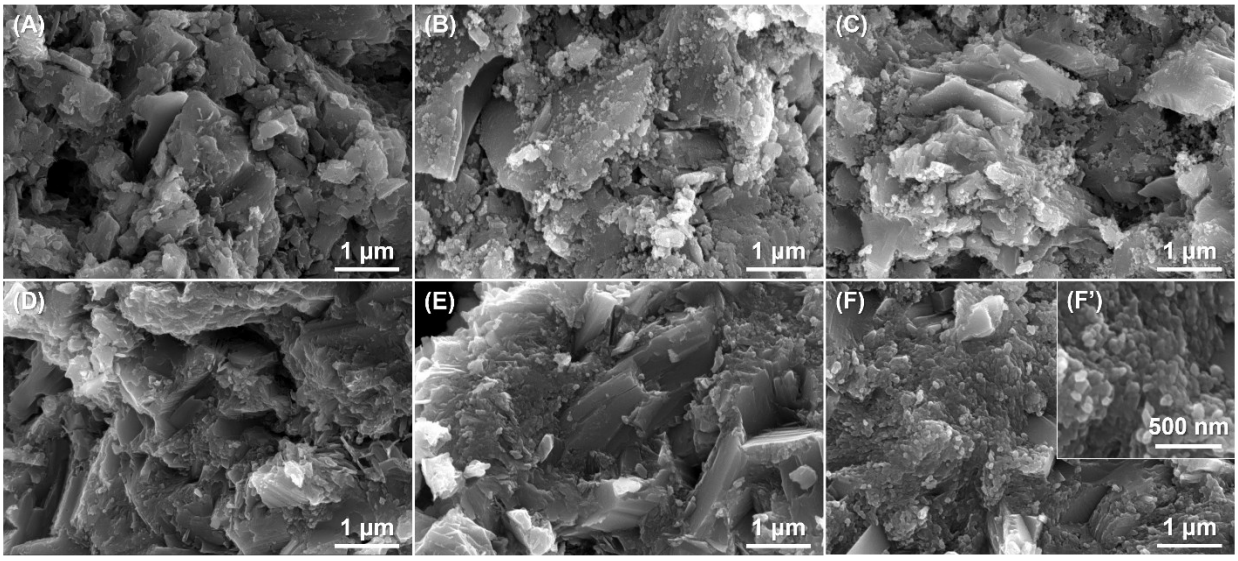

Figure 4. Fractured surfaces of cold sintered diopside with (A) 0 wt%, (B) 10 wt%, (C) 20 wt%, (D) 30 wt%, (E) 40 wt%, and (F) 50 wt% SiO_2 additions, respectively. All specimens were cold sintered using 2 M NaOH for 60-min hold at 200 °C and 400 MPa.

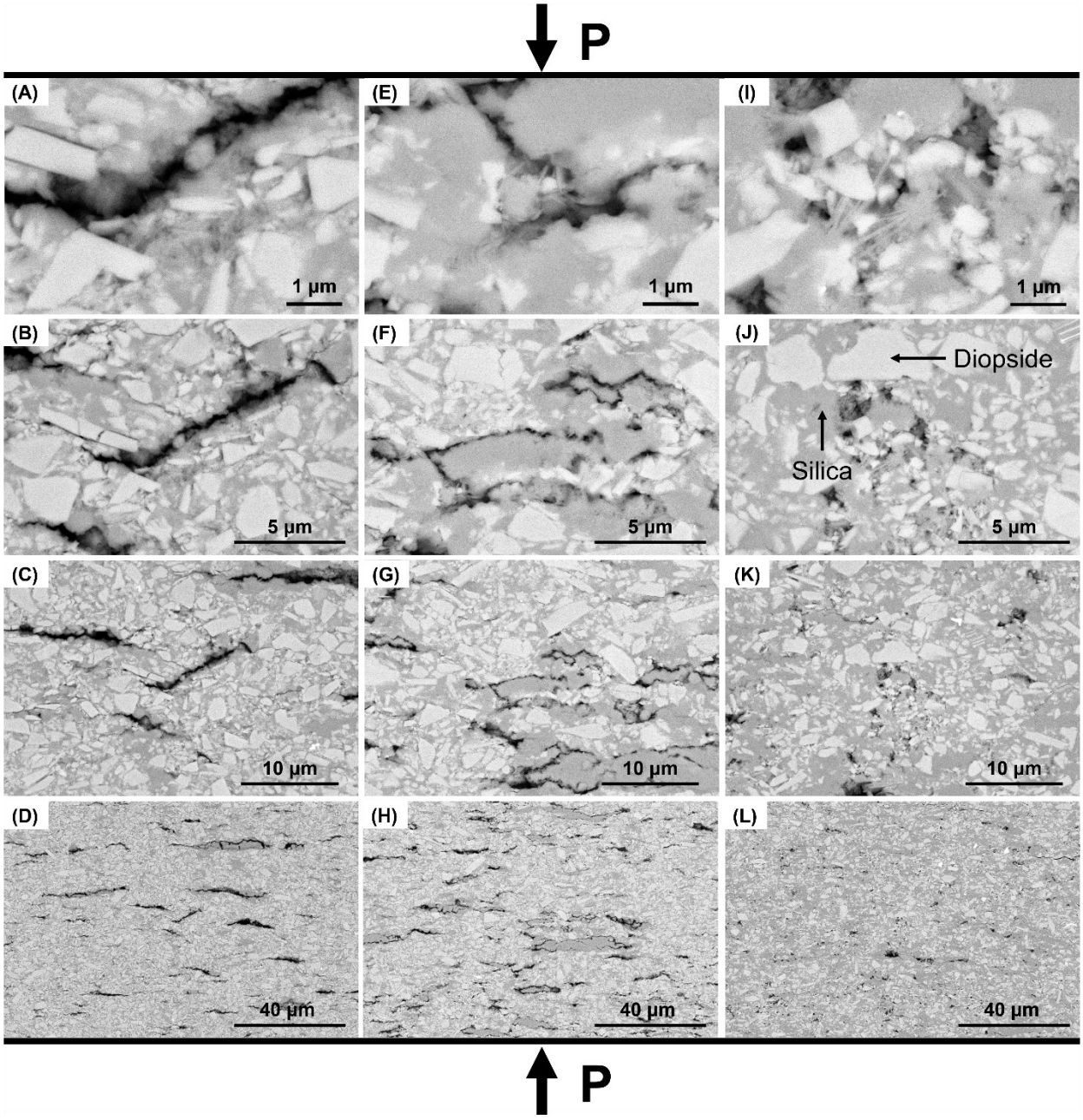

Figure 5. Cross-sectional backscattered electron (BSE) images of cold sintered diopside for (A-D) 30 wt%, (E-H) 40 wt%, and (I-L) 50 wt% silica additions, respectively. Arrows denote the direction of pressing (P) during cold sintering. All specimens were cold sintered using 2 M NaOH for 60-min hold at 200 °C and 400 MPa.

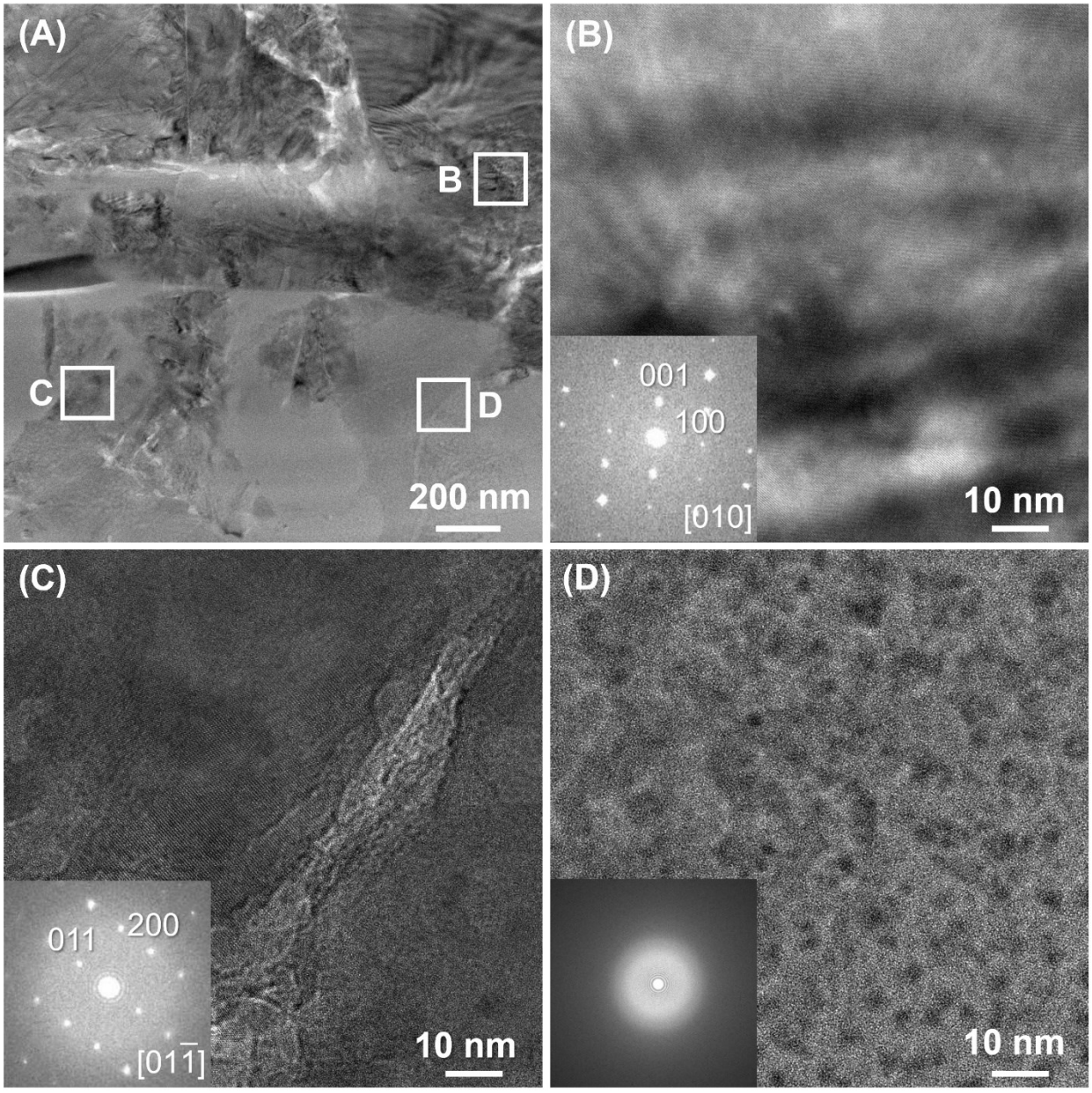

Figure 6. (A) Transmission electron microscopy (TEM) bright-field images of a cold sintered $MgCaSi_2O_6$ + 30 wt% SiO_2 sample, along with selected regions showing (B) quartz, (C) diopside, and (D) amorphous silica. Insets show respective FFT images.

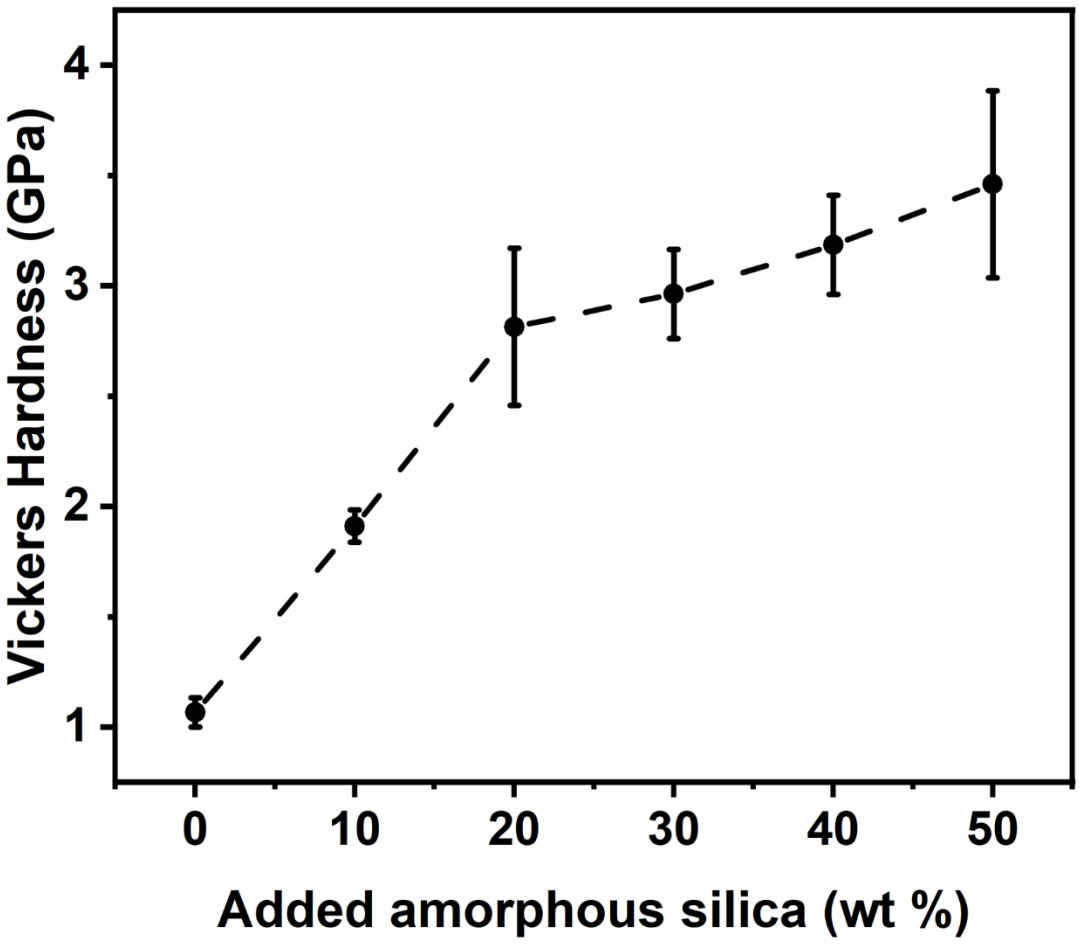

Figure 7. Vickers hardness of cold sintered $MgCaSi_2O_6$ with different amounts of SiO_2 added, measured under the 0.5 kgf load. All specimens were cold sintered using 2 M NaOH for 60-min hold at 200 °C and 400 MPa.

References:

1. Allen, A. J., Thomas, J. J. & Jennings, H. M. Composition and density of nanoscale calcium–silicate–hydrate in cement. *Nat. Mater.* **6**, 311–316 (2007).

2. Wu, J. *et al.* A Generic Framework of Unifying Industrial By-products for Soil Stabilization. *J. Clean. Prod.* **321**, 128920 (2021).

3. Zahabi, M., Said, A. & Memari, A. Cold Sintering of Calcium Carbonate for Construction Material Applications. *ACS Omega* **6**, 2576–2588 (2021).

4. Mei, X. *et al.* Phase transition and dissolution behavior of Ca/Mg-bearing silicates of steel slag in acidic solutions for integration with carbon sequestration. *Process Saf. Environ. Prot.* **159**, 221–231 (2022).

5. Heřmanská, M., Voigt, M. J., Marieni, C., Declercq, J. & Oelkers, E. H. A comprehensive and internally consistent mineral dissolution rate database: Part I: Primary silicate minerals and glasses. *Chem. Geol.* **597**, 120807 (2022).

6. Golubev, S. V., Pokrovsky, O. S. & Schott, J. Experimental determination of the effect of dissolved CO2 on the dissolution kinetics of Mg and Ca silicates at 25 °C. *Chem. Geol.* **217**, 227–238 (2005).

7. Béarat, H. *et al.* Carbon Sequestration via Aqueous Olivine Mineral Carbonation: Role of Passivating Layer Formation. *Environ. Sci. Technol.* **40**, 4802–4808 (2006).

8. Sanna, A., Uibu, M., Caramanna, G., Kuusik, R. & Maroto-Valer, M. M. A review of mineral carbonation technologies to sequester CO_2. *Chem Soc Rev* **43**, 8049–8080 (2014).

9. Funahashi, S. *et al.* Demonstration of the cold sintering process study for the densification and grain growth of ZnO ceramics. *J. Am. Ceram. Soc.* **100**, 546–553 (2017).

10. Gonzalez-Julian, J. *et al.* Unveiling the mechanisms of cold sintering of ZnO at 250 °C by varying applied stress and characterizing grain boundaries by Kelvin Probe Force Microscopy. *Acta Mater.* **144**, 116–128 (2018).

11. Jiang, X. *et al.* Preparation of high density ZnO ceramics by the Cold Sintering Process. *Ceram. Int.* **45**, 17382–17386 (2019).

12. Serrano, A. *et al.* Cold sintering process of ZnO ceramics: Effect of the nanoparticle/microparticle ratio. *J. Eur. Ceram. Soc.* **40**, 5535–5542 (2020).

13. Jiang, P. *et al.* Solid-state Li metal battery enabled by cold sintering at 120 °C. *Mater. Today Phys.* **20**, 100476 (2021).

14. Leng, H., Huang, J., Nie, J. & Luo, J. Cold sintering and ionic conductivities of Na3.256Mg0.128Zr1.872Si2PO12 solid electrolytes. *J. Power Sources* **391**, 170–179 (2018).

15. Lee, W. *et al.* Ceramic–Salt Composite Electrolytes from Cold Sintering. *Adv. Funct. Mater.* **29**, 1807872 (2019).

16. Guo, J. *et al.* Cold Sintering: A Paradigm Shift for Processing and Integration of Ceramics. *Angew. Chem. Int. Ed.* **55**, 11457–11461 (2016).

17. Guo, N., Shen, H.-Z. & Shen, P. One-step synthesis and densification of BaTiO3 by reactive cold sintering. *Scr. Mater.* **213**, 114628 (2022).

18. Ma, J.-P. *et al.* Microstructure, dielectric, and energy storage properties of BaTiO3 ceramics prepared via cold sintering. *Ceram. Int.* **44**, 4436–4441 (2018).

19. Guo, J., Guo, H., Heidary, D. S. B., Funahashi, S. & Randall, C. A. Semiconducting properties of cold sintered V2O5 ceramics and Co-sintered V2O5-PEDOT:PSS composites. *J. Eur. Ceram. Soc.* **37**, 1529–1534 (2017).

20. Zhao, Y. *et al.* Cold-sintered V2O5-PEDOT:PSS nanocomposites for negative temperature coefficient materials. *J. Eur. Ceram. Soc.* **39**, 1257–1262 (2019).

21. Ndayishimiye, A., Bang, S. H., Spiers, Christopher. J. & Randall, C. A. Reassessing cold sintering in the framework of pressure solution theory. *J. Eur. Ceram. Soc.* **43**, 1–13 (2023).

22. Santhosh, B., Galotta, A., Sorarù, G. D., Sglavo, V. M. & Biesuz, M. Cold sintering of colloidal silica particles using different alkali solutions. *Ceram. Int.* **48**, 35627–35632 (2022).

23. Ndayishimiye, A. *et al.* Low temperature hydrothermal sintering process for the quasi-complete densification of nanometric α-quartz. *Scr. Mater.* **145**, 118–121 (2018).

24. Ndayishimiye, A., Tsuji, K., Wang, K., Bang, S. H. & Randall, C. A. Sintering mechanisms and dielectric properties of cold sintered (1-x) SiO2 - x PTFE composites. *J. Eur. Ceram. Soc.* **39**, 4743–4751 (2019).

25. Galotta, A. *et al.* Cold sintering of diatomaceous earth. *J. Am. Ceram. Soc.* **104**, 4329–4340 (2021).

26. Karacasulu, L., Ogur, E., Piskin, C. & Vakifahmetoglu, C. Cold sintering of soda-lime glass. *Scr. Mater.* **192**, 111–114 (2021).

27. Kang, S. *et al.* Evolution from transparent SiO2 glass to ceramics enabled by cold sintering with a transient chemistry: H2SiO3. *Scr. Mater.* **233**, 115522 (2023).

28. Bouville, F. & Studart, A. R. Geologically-inspired strong bulk ceramics made with water at room temperature. *Nat. Commun.* **8**, 14655 (2017).

29. Blair, V., Golt, M., Rosenberger, A. & Hlubb, L. *Cold Sintering of Zinc Oxide (ZnO) and Silica (SiO2)*. https://apps.dtic.mil/sti/citations/trecms/AD1181182 (2022) doi:10.21236/AD1181182.

30. Greenberg, S. A. The Depolymerization of Silica in Sodium Hydroxide Solutions. *J. Phys. Chem.* **61**, 960–965 (1957).

31. Gao, J. *et al.* Realizing translucency in aluminosilicate glass at ultralow temperature via cold sintering process. *J. Adv. Ceram.* **11**, 1714–1724 (2022).